

Coronagraphy with NICMOS

Glenn Schneider

Steward Observatory, University of Arizona, Tucson, AZ 85721 USA

Abstract. The Near Infrared Camera and Multi-Object Spectrometer (NICMOS) provides a coronagraphic imaging capability in camera 2. NICMOS PSF-subtracted coronagraphy routinely results in per-pixel background rejections of $\sim 10^7$ of an occulted target's total flux density at an angular distance of $1''$, thus providing a high-contrast lever for the detection of close sub-stellar companions. At $1.1 \mu\text{m}$ (with an $\sim 0''.1$ spatial resolution), occulted starlight is typically reduced by a factor of 10^5 over a $2''$ - $3''$ annulus, thereby enabling the detection and spatially resolved imaging of low surface brightness material in circumstellar environments. Achieving these performance levels in inherently very high contrast fields while maintaining photometric and astrometric fidelity is challenging and requires careful planning, reduction, calibration and post-processing of coronagraphic imaging data in the presence of residual systematic artifacts. We discuss coronagraphic calibration/processing methodologies developed by the NICMOS IDT (successfully applied to Cycle 7 and 11 data), with recommendations for future observations in light of the ongoing re-verification of NICMOS coronagraphy following SM3B.

1. Introduction

The Hubble Space Telescope (HST) provides a unique venue for high contrast imaging which is further exploited by NICMOS with the incorporation of coronagraphic optics in its intermediate resolution camera (camera 2 with ~ 76 mas square pixels). After internally correcting for the well-known spherical aberration in the *HST* primary mirror, NICMOS+*HST* delivers diffraction limited images with Strehl ratios panchromatically exceeding 98% in the obscured pupil. Moreover, the NICMOS+*HST* PSF is highly stable and repeatable, which permits extremely effective and efficient PSF subtraction. Coronagraphic PSF subtraction is enabled by the high degree of targeting precision afforded by the *HST* pointing control system coupled with autonomous target location and acquisition logic in the NICMOS and *HST* flight software (FSW). Coronagraphically occulted targets are typically positioned "behind" the occulting spot to an accuracy of ~ 8 mas and with a post-acquisition stability of $\sim \pm 4$ mas. Intra-orbit field rotation on sub-orbit timescales (by rolling the telescope around the line-of-sight to the target) permits the identification and rejection of residual optical artifacts. Such artifacts are rotationally invariant in the image plane of the detector, whereas circumstellar features of astronomical origin are not.

The NICMOS detector's multiple non-destructive readout mode (multiaccum) and 16-bit (per read) digital data quantization is well-suited for the high contrast capabilities of its coronagraph (Schneider et al. 1998). Typical multiaccum readout strategies permit a sampling dynamic range of ~ 20 stellar magnitudes in a single visibility period, key to the detection of faint objects in the presence of bright ones.

In *H*-band, the NICMOS coronagraph reduces the background scattered and diffracted energy from coronagraphically occulted targets by factors of ~ 10 at the edge of the $0''.3$ radius occulted region, ~ 4 at $0''.5$ - $1''.5$ and ~ 2 beyond $2''$. After coronagraphic PSF subtraction (i.e., by rotating the field) the background light is further reduced by factors

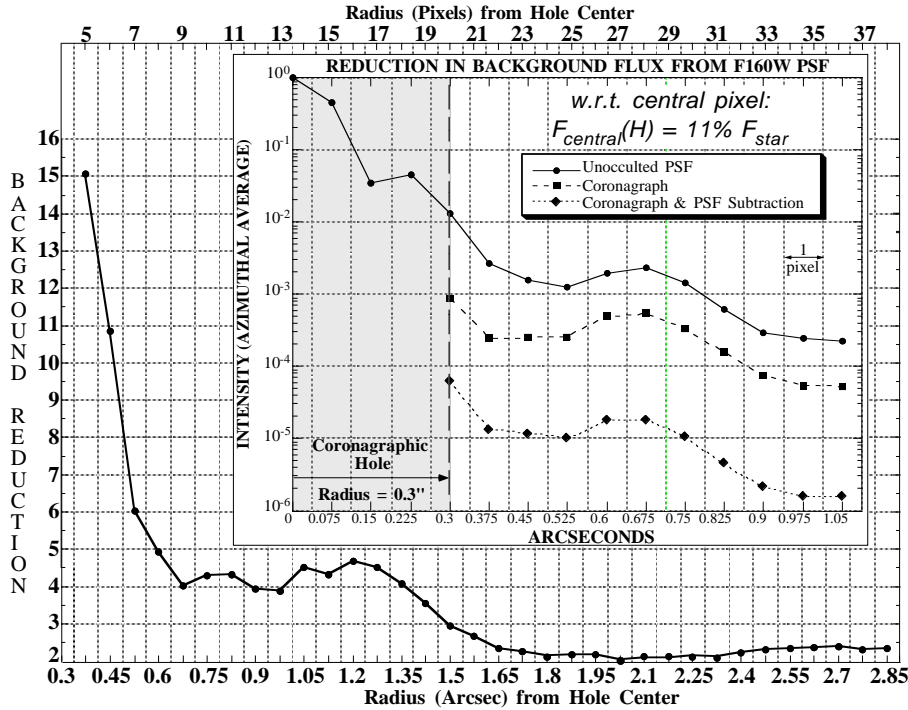


Figure 1. *H*-band coronagraphic stray-light rejection compared to direct imaging. Inset: Per-pixel background relative to central pixel flux density.

of ~ 30 – 50 at $< 1''$, and > 2 orders of magnitude beyond. Together, the background light reduction at $1''$ from an occulted star yields per-pixel background intensities $\sim 10^{-7}$ of the star’s brightness (Figure 1). These performance levels enable the direct imaging of young ($< \text{few} \times 10^7$ years) extra-solar Jovian-mass planets (which decline in luminosity with age) and circumstellar debris disks (with scattering fractions $> 10^{-4}$ at $1''$ or 10^{-5} at $2''$).

These levels of performance were repeatably demonstrated in *HST* Cycle 7/7N and reverified by the recently completed SMOV-3B recommissioning program. Presently, the final on-orbit calibration data required to fully re-enable NICMOS coronagraphy with performance levels achieved in the instrument’s earlier incarnation have not yet been acquired. However, it is clear from the recommissioning tests which have been completed that the coronagraphic system is well within the tunable envelope which will fully enable NICMOS coronagraphy for *HST* Cycle 12 at the same performance levels as demonstrated above.

2. The Coronagraphic Field-Of-View (FOV)

The NICMOS coronagraph is in camera 2, providing 256×256 pixel imaging into an $\sim 19'5 \times 19'3$ FOV with 0.9% X:Y linear geometrical distortion (so images must be rectified before rotationally combined). The coronagraph is optimized for peak performance for wavelengths at and shorter than *H*-band ($1.6 \mu\text{m}$), where the diffracted energy from an unresolved point source in the first Airy ring of its diffraction pattern is fully contained in the coronagraphic “hole” at the instrument’s first image plane. The detector’s FOV is asymmetric with respect to the occulted target. The coronagraphic hole is projected onto the detector image plane $[+73, -45]$ pixels (or $[+5'6, -3'4]$) from the $[-X, +Y]$ corner of the FOV. For two-roll single-orbit imaging (normally with a 30° maximum differential roll due to spacecraft constraints) the total area surveyed around a target is 475 arcsec^2 with an overlap area of 280 arcsec^2 .

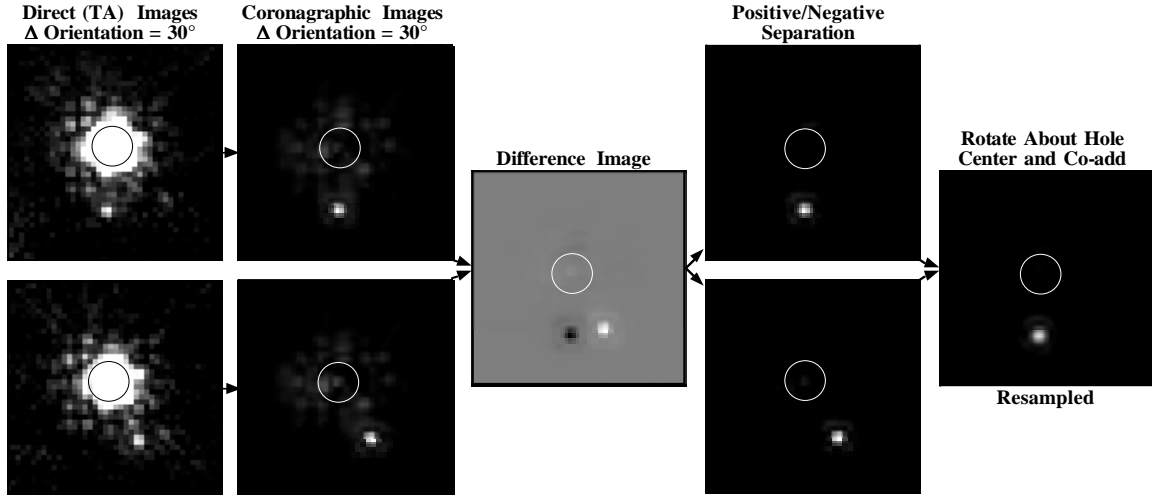


Figure 2. HD 102982 (G3V, $H=6.9$, Lowrance et al. 1998). Two-orientation TA, coronagraphic and PSF-subtracted images, and difference image recombination. Circles indicate size and, except for TAs, location of coronagraphic hole.

3. Coronagraphic PSF Subtraction

In Figure 2 we illustrate the process of NICMOS coronagraphic PSF subtraction for HD 102982, a star with a companion separated by $0''.9$, and a companion:primary H -band brightness ratio of 0.007. Here, following target acquisition (TA) exposures we obtained coronagraphically occulted images of HD 102982 at two spacecraft orientation angles differing by 30° (11 min. total integration time at each orientation). The companion is easily visible in both coronagraphic images, with the fixed speckle pattern in the PSF “wings” of the primary greatly reduced in intensity with respect to direct imaging. In the difference image, the background light from the primary all but disappears. To take advantage of “rotational dithering” which results from image reorientation, we separate the positive and inverted negative components of the difference image and recombine them, after rotational re-registration, resampled onto a sub-pixel grid.¹ The reconstructed image of HD 102982B can be centroided to a precision of ~ 3 mas, and its brightness measured with an internal precision of $\sim \frac{1}{2}\%$.

The total integration time of 11 min. per image orientation was set by the spacecraft and instrument overheads required to execute a two-roll observation in a single visibility period (typically ~ 52 – 54 min.); notably 12 min. for two guide star acquisitions, 11 min. for the spacecraft rotation and 3 min. for two TAs. For most targets of scientific interest, NICMOS coronagraphic observations are not photon or read noise limited, but rather are limited by imperfections in PSF subtraction. In the absence of background light (i.e., sufficiently far from the occulted target), the detection floor for a total integration time of 22 min. was $\sim H = 22.5$ in Cycle 7 (22.9 in Cycle 11; §7.1), though clearly the detection floor is a function of the radial distance from the occulted star. We illustrate this in Figure 3 for a coronagraphic PSF-subtracted (difference) image of LHS 3003 ($H = 9.3$) taken the same manner as HD 102982 but displayed to the noise floor limit.

¹Software for post-processing of calibrated coronagraphic images (IDP3 & DSPK; Schneider & Stobie 2002) is electronically available at: <http://nicmos.as.arizona.edu/software/idl-tools/toollist.cgi>

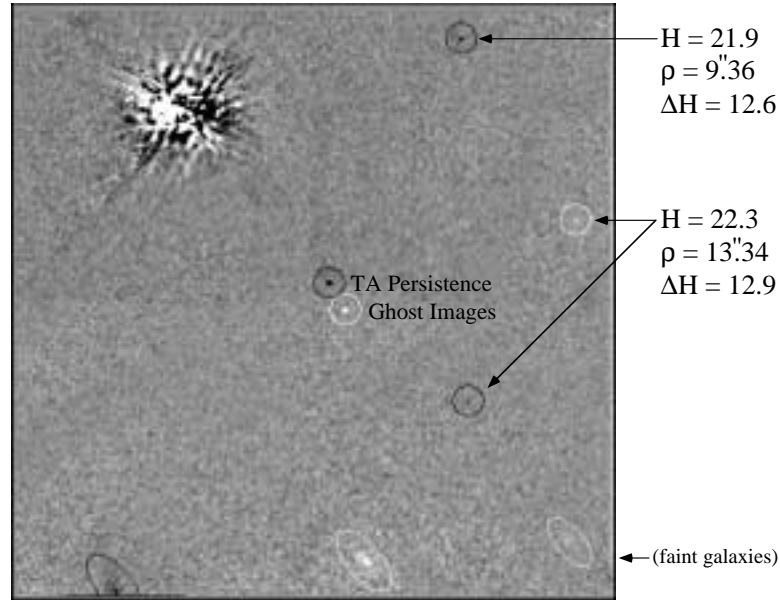


Figure 3. LHS 3003 ($H = 9.3$, M7V). Single visibility period, two-orientation coronagraphic PSF-subtracted faint-object limits at “large” angular separations.

4. Variability of the “invariant” PSF

While the structure of the PSF is highly repeatable, it is not perfectly so. These imperfections arise predominantly from four effects (Schneider et al. 2001). First, changes in the structure of the *HST* PSF arise from variations in the thermal input to the *HST* Optical Telescope Assembly’s (OTA) secondary mirror. As the telescope cycles through orbit day/night, or as it undergoes a major change in attitude or orientation with respect to the Sun, or sub-solar point of the Earth through its orbital phase, the secondary mirror moves by several microns along the optical axis. Though this “breathing” phenomenon (Bely 1993) results in only a small mechanical displacement, it affects the scale and structure of the input PSF illuminating the edge of the coronagraphic hole, which itself acts as a scattering surface. Second, the position of the Lyot stop (pupil plane cold mask) which contributes its own near-field diffraction signature to the final image plane, “wiggles” (Krist et al. 1997) by very small amounts, usually on multi-orbit timescales. Recent data suggest that the amplitude of these motions may be reduced from *HST* Cycle 7/7N (consistent with having been driven by differential stresses in the NICMOS dewar from mass redistribution of the sublimating SN_2). Third, the projected location of the coronagraphic hole onto the image plane of the detector changes with time due to changes in metrology between the NICMOS warm optics and the detector cold bench. The location of the hole is determined by the FSW at the time of each TA, and targets to be occulted are placed with precisions as noted in §1 with respect to the hole. However, changes in the hole and target positions, by even small sub-pixel amounts, result in differential errors in flat-field calibrations and intra-pixel responsivity. Finally, differential targeting errors on the order of a few milliarcseconds can themselves lead to changes in the coronagraphic PSF structure.

Scale changes in the *HST*+NICMOS PSF ultimately affect the coronagraphic sensitivity and detectability dominated by uncompensated background light. Observations of the target and reference PSF should be closely spaced in time, less than the one to several orbit thermal responsivity time constant of the OTA. For two-roll PSF subtractions, where the target serves as its own reference PSF (e.g., for companion detection), this can be accomplished in a single visibility period as previously described.

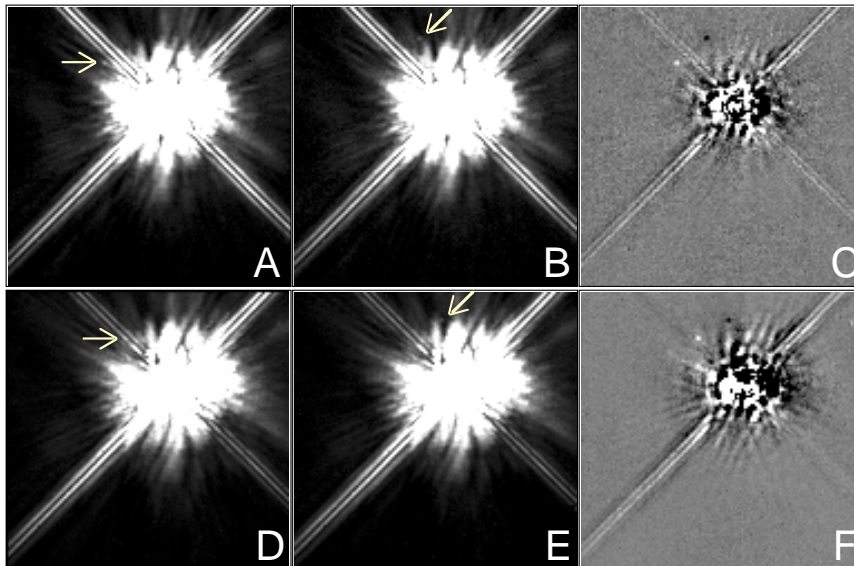


Figure 4. TWA6 ($H = 6.9$, K7V, Schneider & Silverstone 2002). Top: Cycle 7 ($2.19 \mu\text{Jy counts}^{-1} \text{s}^{-1}$), Bottom: Early Cycle 11 ($1.59 \mu\text{Jy counts}^{-1} \text{s}^{-1}$).

5. Pushing the Limits—Companion Detection

We illustrate companion detectability limits in the presence of residual circumstellar starlight first by representative example, and then quantitatively from a statistically significant sample of stars observed in Cycle 7/7N. Figure 4 shows NICMOS coronagraphic images of TWA6 at two image orientations differing by 30° (panels A and B), and acquired in the same manner as the two stars previously discussed. A faint point-like feature is noted even before PSF subtraction in both images. Upon subtraction, a stellar-like (unresolved) object 200,000 times fainter than TWA6 ($\Delta H = 13.2$) appears at an angular distance of $2''.5$ from the occulted star (panel C). The two independent point-like images, each of $S/N \sim 20$, exhibit first Airy-ring structures, core profiles identical to point sources, and are rotated about the occulted target by the field re-orientation angle. This observation is presented as a representative demonstration of capability. Putative companionship must be tested via a differential proper motion measure from two epochs (Figure 4 and §7.1).

We assert the typical nature of the TWA6 observation after assessing the instrumental sensitivity to, and detection probabilities for, identifying nearby companions. Two-orientation PSF-subtracted coronagraphic observations of 50 stars of spectral types G-M, obtained by the NICMOS IDT in *HST* Cycle 7/7N, were subjected to statistical analyses of the radially dependent background noise and star implantation experiments (Schneider & Silverstone, 2002). The systematic noise from imperfect PSF subtractions is azimuthally non-isotropic, as are the sensitivities and detection limits. We find a 50% probability of companion detection of $\Delta H(50\%) = 9.7 \pm 0.3 + 2.1 \times \rho(\text{separation})''$, assuming azimuthally random target placement but with a 30° rotation between two field orientations. The 1σ dispersion of 0.3 magnitudes over the whole sample arises from breathing excursions, target centering errors, and color terms. This may also be cast in terms of the achievable S/N ratio, which we arbitrary quantify at $S/N = 25$ (closely comparable to the TWA6 observation with both rolls combined) as: $\Delta H(S/N = 25) = 8.1 \pm 0.3 + 2.1 \times \rho''$. These levels of performance are highly repeatable for two-orientation PSF subtractions with observations completed in a single visibility period. Specific experiments performed in the *HST* Cycle 7 SMOV 7052 program (Schneider & Lowrance 1997) found degradation in these performance levels of

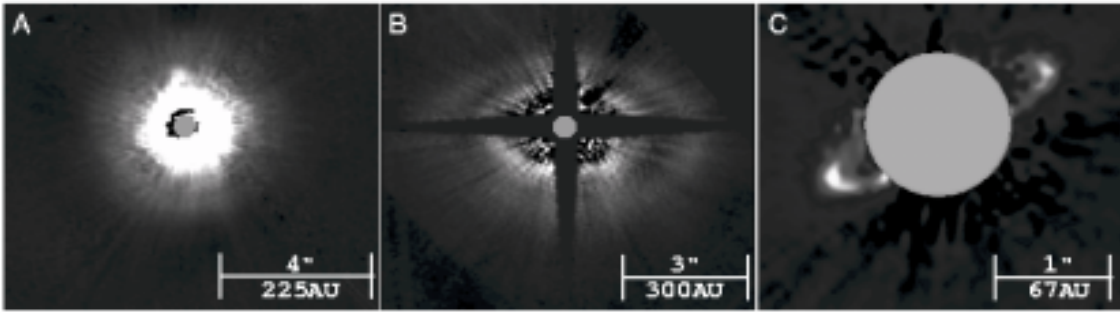


Figure 5. 5–10 Myr debris disks. A: TW Hya (Weinberger et al. 2002), B: HD 141569A (Weinberger et al. 1999), C: HR 4796A (Schneider et al. 1999).

~ 1.5 stellar magnitudes in ΔH for observations taken in sequential orbits rather than in the same orbit, and hence such a multi-orbit observational strategy is contra-indicated.

6. Disk Imaging

Observing light scattered by circumstellar debris has been observationally challenging because of the very high star-to-disk contrast ratios (i.e., low surface brightness disks very close to bright stars). Proto and young circumstellar disks (< 1 Myr) with embedded or obscured central stars may be (and have been) imaged directly. Older, centrally-cleared, disks present a contrast challenge requiring PSF-subtracted coronagraphy (Schneider 2002).

Until NICMOS, the only debris system which had been seen in scattered light was the bright, large, and nearly edge-on disk around β Pictoris. The advent of NICMOS coronagraphy gave rise to the first subsequent scattered light observations of debris disks with a surprising diversity of morphologies and characteristics (Schneider et al. 2002). Dusty disks with radial and hemispheric brightness anisotropies and complex morphologies, possibly indicative of interactions with unseen planetary mass companions, were detected and spatially resolved (e.g., Figure 5). Transitional disks (around Herbig AeBe stars) of intermediate age (1–5 Myrs) have been observed coronagraphically with *HST*/STIS (Grady, 2002), which has been also used for follow-on observations of disks imaged earlier by NICMOS.

In imaging sub-stellar companions, which are spatially unresolved point sources, one can use the host star as its own reference PSF. Circumstellar disks are diffuse spatially extended structures, and the two-roll subtraction technique used for companion detection cannot be exploited. Rather, a reference PSF from a different star must be obtained and used as a surrogate to subtract out the residual instrumentally scattered and diffracted starlight. When a reference PSF is required, a “nearby” star should be chosen to permit a retargeting slew within the same visibility period whenever possible, and such that the Sun angle of the spacecraft does not change significantly. This is sometimes difficult since a PSF star should be at least as bright as the target and of similar spectral type (within one spectral class) to obviate the dominance of color effects (Weinberger 1999). In the worst case a (disk) target and its reference PSF should be observed in subsequent orbits, and at the same orbit phases. To minimize image artifacts resulting from imperfect PSF subtractions, and to sample regions of the disks which will invariably be corrupted by the *HST* diffraction spikes, observations should be obtained at two or more spacecraft roll angles. Image contrast is significantly enhanced for young exoplanet and brown dwarf companion imaging in *H*-band as such objects are self-luminous with higher emissivities at longer wavelength. Disks, however, are seen by the scattering of the central star’s light by circumstellar grains, with color terms, typically, not too different from the stars which

they orbit. For disk surveys it is preferable to image at shorter wavelength, e.g., at $1.1 \mu\text{m}$ (F110W filter), which takes advantage of both the intrinsically higher spatial resolution and the reduced coronagraphically induced instrumental scatter (Schneider et al. 2001). Multi-band imaging with NICMOS can help elucidate the nature of the circumstellar grains, and indeed the camera 2 filter set contains spectral elements which are diagnostic of ices which can mantle such grains at circumstellar distances beyond their sublimation temperatures.

7. Performance Characterization for Cycle 11

With the resurrection of NICMOS in the era of the NICMOS Cooling System we have characterized the performance capabilities of the coronagraph under the SMOV-3B test program. In particular we have evaluated data acquired from the NICMOS TA (8983), Focus Verification (8979) and Initial (Part 1) Performance Characterization (8984) tests. The TA and Focus tests were executed, per the SMOV plan, prior to planned final updates to the NICMOS plate scale and aperture rotation used by the FSW. The initial performance characterization was executed prior to the re-determination and update to the FSW targeting logic’s “low scatter point” in the coronagraphic system. Because the test and update program is not yet completed we cannot present final Cycle 11 (and beyond) performance metrics, though the system “as is” is performing close to the previous mark. Based upon the data acquired at this state of the instrument’s recommissioning, and comparing them to the parameter spaces explored during the SMOV-2 (Cycle 7) program, it is apparent that the NICMOS coronagraphic performance capabilities will be fully restored at the completion of the re-enabling activities (to be carried out under the Cycle 11 calibration plan).

7.1. TWA6 Revisited

As a demonstration of restored capability, we re-observed TWA6 “out-of-the-box” as part of the NICMOS TA testing. In Figure 4 we compare Cycle 7 (top) and Cycle 11 (bottom) coronagraphic images to illustrate the high degree of repeatability of the NICMOS coronagraphic PSF after a more than three year suspension of activity. The point object seen in the Cycle 7 observation is seen at nearly the same image contrast as in the Cycle 11 observation. The Cycle 7 and 11 images were acquired at slightly different absolute orientation angles, so the point object is at slightly different azimuthal angles at the two epochs (and is co-incident with the occulted star’s (-X,-Y) diffraction spike in panel D). To first order, the system performance is roughly comparable. Residual optical artifacts (i.e., radial streaks extending to $\sim 2''$) are more prominent in the Cycle 11 PSF subtracted image. This is a consequence of differential targeting errors between the two image orientations and is a direct result of executing this test before later-planned on-board calibration updates. This is fully within the envelope of correction of the planned updates and will be mitigated following the completion of Part 2 of the coronagraphic performance characterization test.

In Cycle 11 (NCS at 77K), the pixel-to-pixel (read) noise is lower in amplitude, relative to the photon flux from an occulted target (and field object) as compared to Cycle 7 (SN₂ at 62K). This improvement arises from an increase in *H*-band quantum efficiency (QE) of $\sim 37\%$ (Figure 4). For comparative purposes the Cycle 7 and 11 images have been stretched to permit direct comparison in light of the net gain in imaging efficiency.

In both the Cycle 7 and Cycle 11 observations we were able to measure the positions of the unresolved object to a precision of ~ 11 mas with respect to TWA6. Over the 4 yr temporal baseline, the angular distance decreased by 160 mas in the direction expected from the proper motion of TWA6 itself, implicating a background object rather than a Jupiter-mass companion to this 10 Myr star (unfortunately). However, these two-epoch observations demonstrate the ease with which such observations can be reliably and repeatably made.



Figure 6. A: OTFR/CALNICA pipeline reduction with synthetic dark and library flats, B: CALNICA with custom-matched dark and linear-regime flat-field.

8. Calibration

The performance levels discussed assume properly calibrated and cosmetically clean data. Whether searching for companions or circumstellar disks, local and global deviations from true photometric backgrounds must be corrected (zeroed) before PSF subtraction. Failure to appropriately do so will result in: loss of sensitivity (against the residual background); degraded detectability in PSF-subtracted images; photometric zero-point errors; and spatially non-uniform detection limits. With coronagraphic data, in particular, one must be critical of pipeline processing.

Standard reference flats from STScI’s calibration database system contain a static imprint of the coronagraphic hole though the position of the hole is known to be unstable at the level of roughly a pixel. Before flat-fielding high-S/N reference flats should be augmented with contemporaneous ($S/N \sim 130$ combined) lamp flats, provided as part of the TA process, otherwise very significant near-hole flat-field gradients may arise. We also suggest that reference flats be constructed so as not to rely on assumed high-fidelity knowledge of the per-pixel linearity transfer when approaching saturation. I.e., discard non-destructive reads in raw flat-field frames with pixel values $> 50\text{--}70\%$ full-well when making reference flats.

The efficacy of using “synthetic” (decomposed model) darks (currently generated by OTFR) vs. reference dark frames made directly from observed calibration frames is somewhat conjectural and may be data driven. Preliminary indications from Cycle 11 data are that synthetic darks in many cases may suffice as the NICMOS detectors (which have temperature dependent dark currents) are now thermally more stable than in Cycle 7. Manual (and sometime laborious) construction of dark reference files from Cycle 7 data which are selected to match (1) the temperature of the detector at the time of the observation (as reported in the SPT file), and (2) the relative time from the prior SAA exit, often reduce photometric errors relative to the Cycle 7 model darks. Fortunately, two-roll per visibility observations are inherently SAA non-interruptible, so usually they are less subject to degradation from cosmic-ray induced excess dark current decays from prior SAA crossings.

As an example, in Figure 6, we show the result of re-processing a raw NICMOS coronagraphic frame using OTFR/CALNICA compared to an IDL-based analog to CALNICA using reference darks made from selected, observed, data, flats unreliant on linearity corrections, and Gaussian-weighted bad pixel replacement. Post-processing tools exist in the IRAF/STSDAS environment to mitigate calibration errors (such as in the example shown),

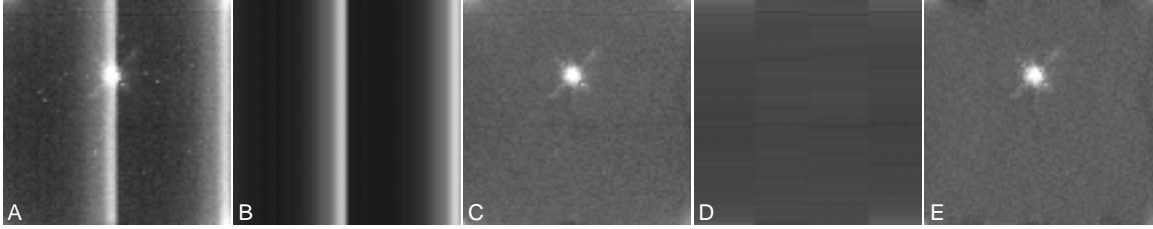


Figure 7. A: Raw TA image, B: Shading model, C: Shading removed (and bad pixels replaced), D: Bars model, E: Bars removed.

but they often do not work well in regions of high flux densities and large signal gradients which fill the field (e.g., for bright coronagraphic targets). Experimentation is required, and improvements over pipelined results can be had with this additional work.

9. Mode-2 Target Acquisition Data

Though often under-appreciated, data which are taken (and delivered) from TAs are of fundamental importance in the calibration and interpretation of coronagraphic imaging data which follow. TA images serve as astrometric anchors, and are required to accurately determine the placement of a target into the coronagraphic hole. Such determinations cannot be made from coronagraphic images themselves. In *HST* Cycle 7 targeting information from the spacecraft slew, which put the target into the coronagraphic hole, was reported in the ancillary SPT file (first in raw engineering units, later in detector pixels). In Cycle 11 the OTFR pipeline has been updated to place this information in the FITS headers of the RAW and CAL files themselves, but co-ordinates are still given in the FSW’s detector pixel system, not in the science instrument aperture system (SIAS). For camera 2: $SIAS[X,Y] = 256-FSW[Y,X]$. The information provided through these files, however, uses the fixed aperture “constants” (scale and rotation) employed by the FSW, though these may change over time. For highly accurate astrometry, the TA information reported in the FITS headers may require updating to reflect the actual “plate constants” at the time of the observation. Such information historically has been provided by STScI through a web-based interface.²

With the improved detector QE in Cycle 11, stellar PSF cores will not saturate at the shortest (0.2s) TA exposure times for the recommended TA filters as follows: F160W: $H > 7.2$; F165M: $H > 6.5$; F171M: $H > 5.5$; F187N: $H > 4.0$. For targets with $H < 4$, Mode-1 TAs are needed. Autonomous acquisition of targets of $H > 18$ are prone to failure as such targets are difficult to discriminate from hot pixel clusters by the on-board software.

Properly exposed ($\sim 70\%$ full-well) TA images can be used to establish an in-band magnitude for the filter used. Additionally, “hole location” lamp-flat background images are taken (as two 7s ACCUM images) and may be used to ascertain the H -band magnitude of an unsaturated target, even if the TA was done in a different filter. Color transformation from a TA or lamp-background filter to a different science filter may be estimated by using STSDAS SYNPHOT task. These serendipitous photometric determinations may not be optimal. Whenever possible, unocculted images of subsequently occulted targets should be obtained as part of the planned imaging sequence to establish the PSF core photometry. This is particularly necessary for disk imaging where the in-band flux ratios of the target and reference PSF must be known to obtain a proper scaled PSF subtraction.

TA ACCUM mode images, F160W lamp flats and background images (which will contain an image of the star to be acquired) are not calibrated by the OPUS pipeline.

²<http://www.stsci.edu/hst/nicmos/performance/platescale>

Dark current is usually not an issue for short TA images and lamp background frames (but may be so for hot pixels), but the detector reset signature (aka “shading”) will bias target concentrations with horizontal field gradients, and introduce photometric errors amplified through the flat-field. TA images are also subject to a readout anomaly known as “the bars”, which though correctable, are not handled by the OPUS pipeline. TA images may be calibrated by: (1) pixel-paired minimization to eliminate cosmic rays, (2) building a source-clipped (or masked) column-median to characterize and build a 2D shading image to be subtracted, (3) building a source-clipped row-median image to eliminate the bars upon subtraction, (4) flat-fielding with a library (or contemporaneous TA) flat. Alternatively to (1), multiaccum darks could be taken, but because of subtle differences in detector clocking compared to TA/ACCUM mode the integration time should be increased by +0.025s.

10. Summary

The SMOV-3B program has demonstrated a full return of NICMOS coronagraph science capabilities with stray-light rejection closely replicating Cycle 7 performance. Coronagraphic detection limits, with and without PSF subtraction, will be fully restored after planned updates to the FSW’s TA calibration constants have been made. System sensitivities have increased ($\sim 37\%$ in *H*-band) due to the higher QE of the detector now operating at 77K. Final refinements to performance metrics and calibration data await the completion of the Cycle 11 calibration plan. NICMOS is ready to resume coronagraphic science in Cycle 12.

Acknowledgments. This work is supported by NASA grants NAG5-3042 and 10843. We thank M. Silverstone and J. Beattie for a careful proof reading of this manuscript.

References

- Bely, P. 1993, STScI Report (SESD-93-16)(Baltimore: STScI)
Grady, C. 2002, this volume, 137
Krist, J. E., et al. 1998, PASP, 110, 1046
Lowrance, P. J., et al. 1998, ESO Conf. Proc., 55, 96
Schneider, G. & Lowrance, P. 1997, SMOV/7052 Test Report,
http://nicmosis.as.arizona.edu/gschneid/7052_PS/
Schneider, G., Thompson, R. I., Smith, B. A., & Terrile, R. J. 1998, Proc. of SPIE, 3356, 222
Schneider, G., et al. 2001, AJ, 121, 525.
Schneider, G. & Stobie, E. 2002, ASP Conf. Ser. 281, in press
Schneider, G. 2002, in Hubble’s Science Legacy: Future Optical-UV Astronomy From Space, ed. C. Blades, ASP Conf. Series, in press
Schneider, G. & Silverstone, M., 2002, Proc. of SPIE, 4860, in press
Schneider, G., Weinberger, A. J., Silverstone, & M. D. Cotera, A. S. 2002, in Debris Disks and the Formation of Planets, ed. D. Bachman, ASP Conf. Series, in press
Weinberger, A. J., et al. 1999, ApJ, 522, L53
Weinberger, A. J., et al. 2002, AJ, 566, 409